A&A 411, L159–L166 (2003)
DOI: 10.1051/0004-6361:20031439

Astronomy & Astrophysics

IBIS ground calibration

A. J. Bird[1], E. J. Barlow[1], A. Bazzano[2], C. Blondel[3], M. Del Santo[2], G. Di Cocco[4], M. Gabriele[5], P. Laurent[3], F. Lebrun[3], G. La Rosa[5], G. Malaguti[4], E. Quadrini[6], A. Segreto[5], T. Tikkanen[1], P. Ubertini[2], and R. Volkmer[7]

[1] School of Physics and Astronomy, University of Southampton, Highfield, Southampton, SO17 1BJ, UK
[2] Istituto di Astrofisica Spaziale e Fisica Cosmica, IASF/CNR, Rome, Italy
[3] Service d'Astrophysique, Sap-CEA, Saclay, France
[4] Istituto di Astrofisica Spaziale e Fisica Cosmica, IASF/CNR, Sezione di Bologna, Bologna, Italy
[5] Istituto di Astrofisica Spaziale e Fisica Cosmica, IASF/CNR, Sezione di Palermo, Palermo, Italy
[6] Istituto di Astrofisica Spaziale e Fisica Cosmica, IASF/CNR, Sezione di Milano, Milan, Italy
[7] Institüt für Astronomie und Astrophysik, Tübingen, Germany⋆

Received 11 July 2003 / Accepted 16 September 2003

Abstract.
We present an overview of results obtained from IBIS ground calibrations. The spectral and spatial characteristics of the detector planes and surrounding passive materials have been determined through a series of calibration campaigns. Measurements of pixel gain, energy resolution, detection uniformity, efficiency and imaging capability are presented.

Key words. INTEGRAL – gamma-ray – calibration

1. Introduction

The IBIS telescope on board INTEGRAL (Ubertini et al. 1996; Winkler et al. 2003) features a highly pixellated detector system with an extremely complex response, and there has therefore been a major activity to perform a full on-ground calibration prior to launch.

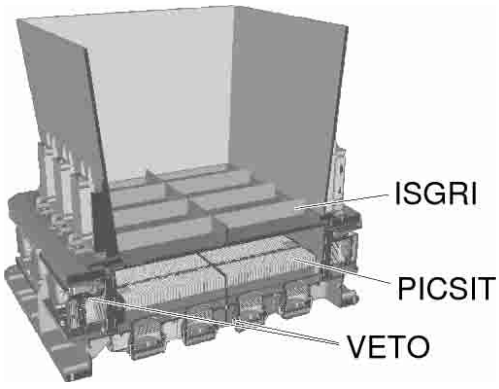

Fig. 1. Cutaway of the IBIS detector assembly, showing the detector planes and shielding systems.

The IBIS detector assembly (Fig. 1) consists of two large pixellated detector planes surrounded by a combination of active and passive shielding. The uppermost detector plane, ISGRI, consists of a 128×128 array of CdTe pixels, each $4 \times 4 \times 2$ mm in size (Lebrun 2003). The lower detector plane, PICsIT, consists of 64×64 pixels, each a $8.4 \times 8.4 \times 30$ mm CsI(Tl) scintillator read out at one end by a PIN photodiode (Labanti 2003). The ISGRI and PICsIT detectors are arranged in 8 independent modules, with a separate channel of readout electronics for each pixel. The detector planes are surrounded by an active shielding system consisting of 16 veto modules (8 lateral, 8 rear), each one a large BGO scintillator read out by two photomultipliers (Quadrini 2003). An additional passive shield is used to define the field of view of the instruments at low energies.

2. Calibration philosophy

IBIS was subjected to a rigorous course of calibrations throughout and after its construction in order to verify the scientific performance of the detector systems and produce inputs to the process of instrument response generation. In addition, due to the lack of a true flight spare, the calibration results are providing an archive of data which cannot be recreated now the instrument is in-flight.

The key aims of the calibration process were:

– optimisation of instrument parameters. A *Science Optimisation* phase was conducted after each phase of functional tests and before each calibration campaign in order to set the instrument in the best condition for calibration;

Send offprint requests to: A. J. Bird,
e-mail: ajb@astro.soton.ac.uk
⋆ Now at KIS, Freiburg, Germany.

– measurement and verification of the instrument scientific performance;
– determination of instrument characteristics as input for on-board and ground look-up tables (LUTs);
– provision of inputs to response matrix generation (in combination with modelling).

2.1. Calibration campaigns

The IBIS ground calibration was conducted in a series of distinct phases which coincided with the instrument development program. The calibration plan, written early in the programme, was used to identify the optimum stage(s) of the calibration for each test. All flight subsystems were tested *in isolation* before integration began, after which the integration and calibration of the telescope continued in parallel. Early tests allowed for more flexible access to the detector planes, while tests on the final flight configuration were necessarily more limited in scope. The detectors and mask were only calibrated together for the ESTEC tests onwards. The Payload-Level Ground Calibration (PLGC) campaign represented a major part of the overall calibration philosophy.

Table 1. IBIS calibration campaigns.

Phase	Date	Location
Subsystem	2001	Various
Instrument	Nov. 2001	Laben
Instrument	Dec. 2001	ESTEC
Payload (PLGC)	Jan./Feb. 2002	ESTEC
Thermal-vacuum tests	Apr./May 2002	ESTEC

2.2. Calibration configuration

Calibration measurements were made, where possible, with the instruments in photon-by-photon mode so as to retain the maximum information in the calibration data. With IBIS in photon-by-photon mode, separate event lists are received in telemetry for ISGRI events, ISGRI calibration events, Compton-mode events (simultaneous ISGRI and PICsIT detections which are assumed to have scattered between the two detector planes), PICsIT events and PICsIT calibration events. Both Compton and PICsIT events are further subdivided into single and multiple events: in either case, a multiple event is defined as one that interacts in more than one PICsIT pixel.

However, the high level of information present in photon-by-photon mode data was in conflict with the strict data-rate limits imposed by the telemetry system. In-flight, much of the telemetry requirement is reduced by using on-board histogramming of the PICsIT data. During the on-ground payload calibration, where relatively strong sources were used, a Fast Acquisition System (FAS) was used to bypass the normal telemetry stream for photon-by-photon science data, thus allowing much larger datasets to be collected.

When tests required the use of on-board event selection, control measurements were always made with an absolute minimum of on-board processing, again to minimise the chances of unknown effects biasing the calibration datasets and to retain maximum information.

Point-like radioactive sources were used to illuminate the detectors, either via flood illumination or using a selection of collimators, providing a range of twenty separate lines from 22 to 2754 keV. An X-ray generator was used during payload calibration to provide intense fluxes in the range 17–120 keV.

In addition, through all campaigns, initial long and repeated short background runs were used to maintain a record of background conditions and to allow background subtraction where required.

Unless otherwise stated, tests were performed with the ISGRI bias set to 100 V, and PICsIT bias at 20 V. All tests, with the exception of the thermal-vacuum tests, were performed at a standard temperature of 20 °C.

3. Parameter optimisation

The *Science Optimisation* phases prior to Laben and PLGC calibration campaigns were used to tune various critical instrument parameters (Table 2). These principally concern the various strobe signals which are used to communicate coincident detections between different detector subsystems. For each strobe, a delay (the time difference between the response of the two systems) and strobe width (to compensate for timing jitter and energy dependences) must be set.

Table 2. Optimised parameters.

VETO-ISGRI strobe delay	9 μs
VETO-ISGRI strobe width	2 μs
VETO-PICsIT strobe delay	6.5 μs
VETO-PICsIT strobe width	2.0 μs
ISGRI delay in HEPI	2.5 μs
PICsIT delay in HEPI	0.0 μs
ISGRI-PICsIT coincidence window	4.0 μs

These values were used to determine the configuration during ground calibration, and also as a starting point for the in-flight commissioning.

4. Spectral characteristics

The IBIS instruments combine to produce a wide energy response. During ground calibrations, ISGRI was operated with a threshold of ~15 keV, and PICsIT with a threshold of ~175 keV. The response of ISGRI extends to ~800 keV, while PICsIT nominally extends to 10 MeV. The Compton mode (simultaneous ISGRI and PICsIT events) operates in a similar range: 190 keV–10 MeV.

When measuring the spectral characteristics of the CdTe detectors in ISGRI, it is important to consider the role of charge trapping in the detector material. Each energy deposit in the detectors is subject to a degree of charge trapping, largely dependent on the depth of interaction within the detector. In ISGRI, the amount of charge trapping is determined by measurement

of the rise-time of the detector pulse (Lebrun et al. 2003). Pulses with the longest rise-time have been subject to the greatest charge loss, and so have the largest uncertainty in their energy determination. ISGRI calibration may be performed on the raw pulse height analysis (PHA) values, a rise-time selected subset of the PHA values, or the charge-loss corrected (usually referred to as pulse invariant (PI)) values.

For Compton mode data, combination of ISGRI and PICsIT pulse height information can only be meaningfully accomplished after conversion of the ISGRI PHA values to charge-loss corrected energy values.

4.1. Linearity

The instruments display excellent linearity over the full energy range (Fig. 2).

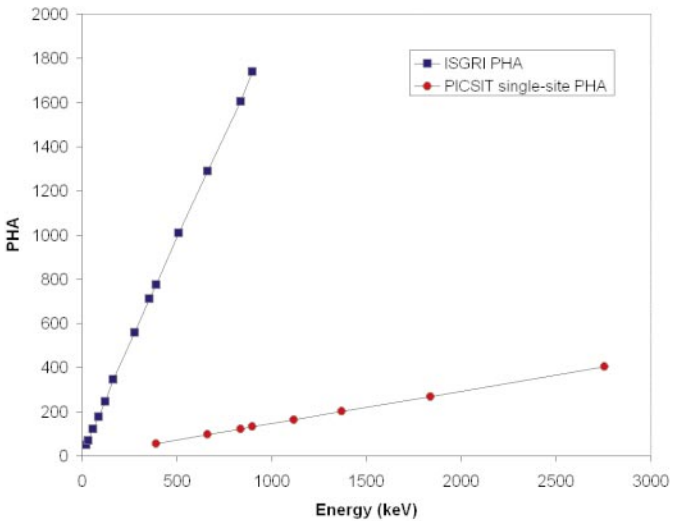

Fig. 2. Energy linearity (pulse height v. energy) for ISGRI and PICsIT detections.

In the study of ISGRI linearity, mean photopeak pulse height (PHA) values have been derived following selection of only those events with very low rise time, such that the effects of charge trapping are minimised i.e. those events with only minimal charge loss. For this subset of events, the photopeak in the pulse height sepctrum is still Gaussian in shape and shows little of the low-energy tailing characteristic of CdTe detectors.

For PICsIT, the smaller number of pixels allowed for collection of better statistics at pixel level, and pixel gain normalisation is already applied in the telescope. Thus a simple Gaussian function was fitted to the photopeak in each pixel spectrum, and the mean peak position over the whole detector plane was computed.

It should be noted also that the ISGRI and PICsIT PHA–energy relationships are very different in order to cope with the different dynamic ranges required of the two detector planes.

4.2. Energy resolution

The energy resolution as a function of energy has been determined (Fig. 3).

For analysis of ISGRI energy resolution, gain/offset correction was made for each energy deposit based on which pixel it interacted in (so as to normalise the gain of all pixels). A spectrum was compiled summing all the events in all the pixels, and a simple measurement of full width at half-maximum (FWHM) was made on the photopeak. This method is only valid at relatively low energies, where the effects of charge loss are minimal.

For PICsIT, as for the linearity measurement, analysis was performed by line fitting at pixel level.

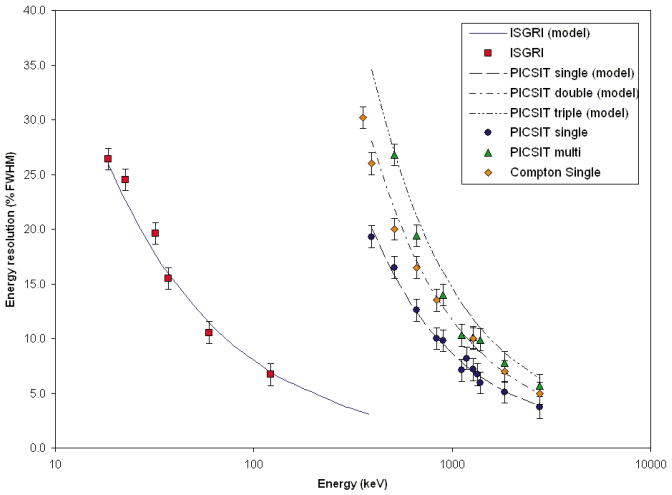

Fig. 3. Energy resolution as a function of energy for ISGRI, PICsIT and Compton detection modes.

The energy resolution for the detectors has been characterised by models, which are also shown in Fig. 3. PICsIT multiple events are a mixture of 2-site and 3-site events, and thus the energy resolution appears, as expected, between the models for pure 2-site and pure 3-site events (calculated assuming an even share of energy between the interactions).

For ISGRI, despite the complex energy response, a simple empirical model provides an adequate description at low energies:

$$\frac{\Delta E}{E} = 200 \times E^{-0.7} \quad (\%\ \mathrm{FWHM}) \tag{1}$$

where E is the energy deposit in keV. For PICsIT, a physics-based model is useful since it allows the pixel performance to be assessed:

$$\frac{\Delta E}{E} = 2.35 \times \frac{\sqrt{nE + N^2}}{nE} + k \quad (\%\ \mathrm{FWHM}) \tag{2}$$

where N is the electronic noise (typically 950 electrons rms), n is the number of electrons/keV created in the CsI(Tl) scintillator (typically 29.1) and E is the energy deposit in keV. k is an intrinsic resolution term caused by variations of light output and collection within a pixel, and has a typical value of 1.7%.

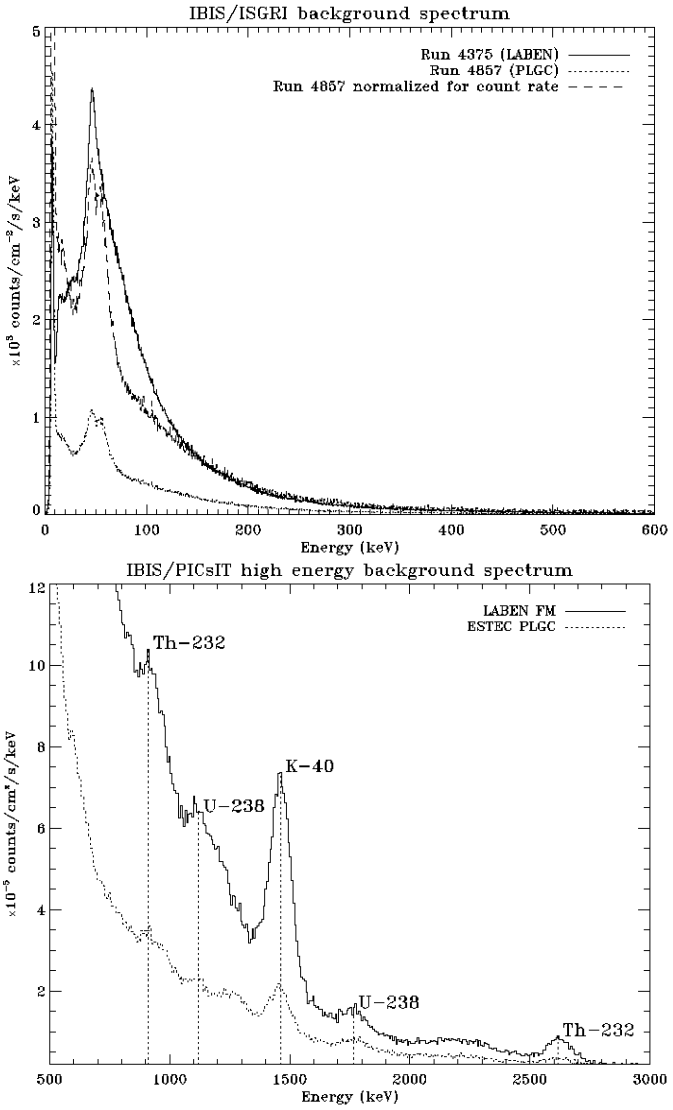

Fig. 4. ISGRI and PICsIT background spectra measured during the detector assembly and payload calibration phases.

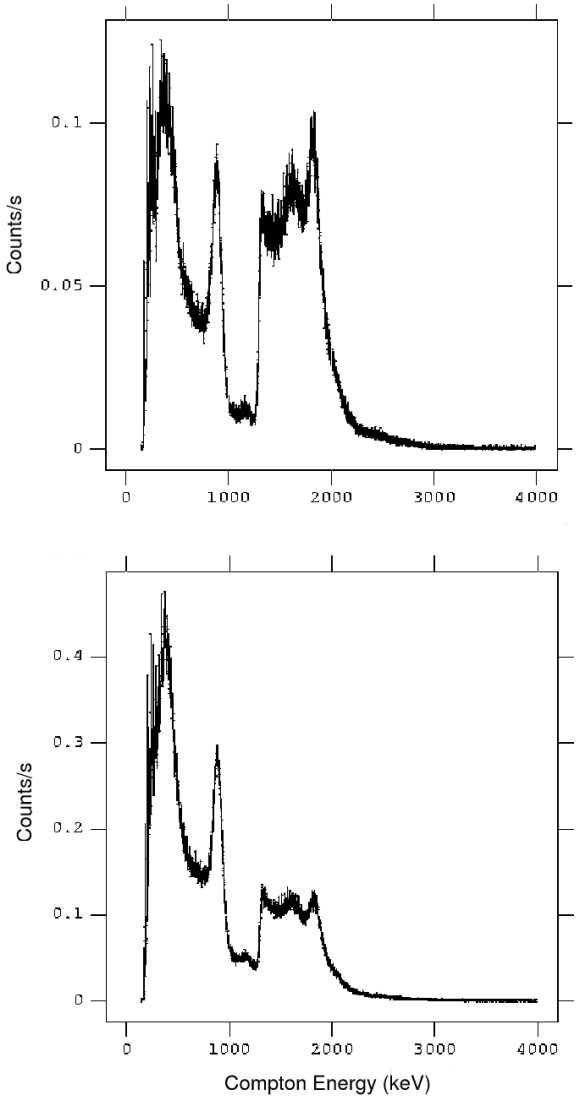

Fig. 5. Compton spectra (^{88}Y source) for (top) 5°, and (bottom) 15° selection angle.

As an example of the broad-band spectral capability, Fig. 4 shows the ISGRI and PICsIT background measured at Laben and ESTEC.

Each spectrum is the result of a ~2000 s exposure, summed over all the pixels in the relevant detector plane. In the ISGRI spectrum, the dominant features are from fluorescence of passive material surrounding the detector field of view. This is particularly clear in the PLGC spectrum where the peaks from both the tungsten hopper and lead tube are visible. The PICsIT spectrum is dominated by lines from environmental ^{238}U→^{232}Th→^{40}K chain decays. In both cases the background in the PLGC configuration, with the full shielding in place, is much lower than for the detector plane calibrations at Laben.

Compton mode data have also been analysed to evaluate the spectral characteristics. Each Compton event consists of one energy deposit in ISGRI, simultaneous with one or two energy deposits in PICsIT. The energy resolution for Compton events therefore has been derived by independent correction of the ISGRI and PICsIT components followed by simple summation of the two contributions, and is shown in Fig. 2. Figure 5 shows two typical Compton pulse height spectra for Compton-single events (one event in ISGRI and one event in PICsIT). Apart from the usual features attributable to a ^{88}Y source emitting lines at 898 keV and 1836 keV, the most notable feature is a sharp discontinuity at 1.3 MeV, which was the threshold energy for Compton event selection during these acquisitions.

The events below the Compton selection threshold are subjected to an on-board event selection algorithm designed to remove Compton events which originated from outside of a cone centred on the telescope axis. The size of the acceptance cone (the selection angle) may be configured to optimise the rejection of background while minimising the effect on source photons. Comparison of the two spectra in Fig. 5 shows the reaction to changes in the Compton selection angle. In the two acquisitions, the selection threshold is constant at 1.3 MeV while the selection angle, which determines the severity of the

selection, changes from 5° to 15°. As expected, the count rate above the threshold is unaffected by changes in selection angle, while the counts below the threshold are further suppressed for 5° selection. Noticeably, the source counts are also attenuated, although not as strongly as the background. The relatively small distance to the source means that it appears significantly off-axis for much of the detector plane, and the rejection algorithm is not optimised for that case. Nevertheless, the fraction of background events rejected agrees extremely well with simulations.

5. Spatial characteristics

5.1. Threshold distribution

For ISGRI, the threshold of each pixel is determined automatically during the low threshold adjustment (LTA) phase of instrument initialisation, and the thresholds are transmitted in the instrument context. Figure 6 shows the distribution of ISGRI pixel thresholds after LTA.

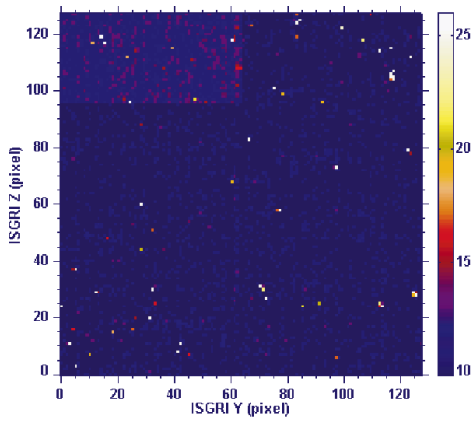

Fig. 6. ISGRI threshold distribution after LTA. One threshold step is equivalent to ~1.23 keV.

The threshold distribution is rather uniform; even though one detector module is clearly slightly different, it is only by on average two threshold steps (~2.5 keV). A few pixels have been correctly identified as noisy, and have much higher thresholds set.

For PICsIT, the thresholds are set in hardware at semi-module level, but vary from pixel-to-pixel due to gain and offset variations. The actual threshold may be determined from the event or histogram data itself (Fig. 7).

The semi-module structure can be seen in the map of PICsIT pixel thresholds, but again, the threshold distribution is perfectly acceptable with a mean value at ~175 keV.

5.2. Noisy/dead pixels

In ISGRI, the number of pixels switched off as "noisy" was seen to evolve during each acquisition until it reached a stable equilibrium. Figure 8 shows the evolution of noisy pixel number over a period of ~8 hours, starting from a period of

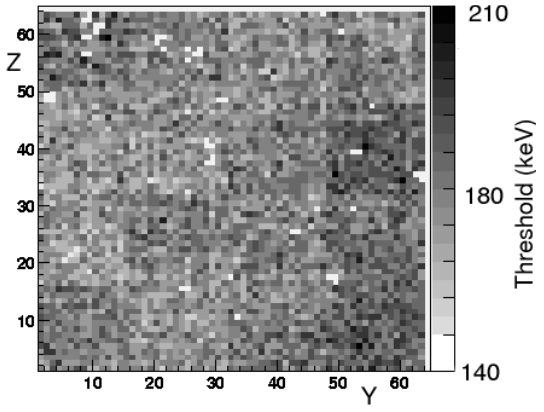

Fig. 7. PICsIT pixel threshold distribution.

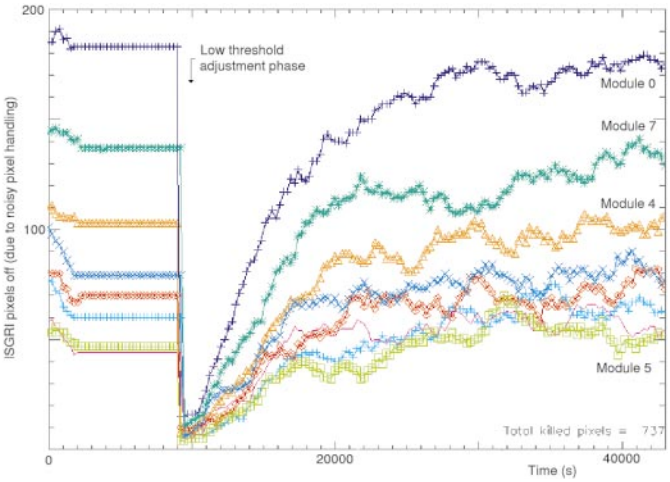

Fig. 8. Noisy pixel evolution. Each line represents one ISGRI detector module containing 2048 pixels.

equilibrium, followed by a period of low threshold adjustment which resets the noisy pixel status, and finally the slow increase to equilibrium again.

At equilibrium, there are ~725 noisy pixels turned off at any one time. This is not a severe problem, representing at most ~4% of the total ISGRI pixels. Since they are distributed approximately randomly, this has negligible impact on the imaging process, and since the times at which the pixels are turned on and off are known, the effective area is well defined. The physical cause of the noisy pixels is still being investigated, but it is clear that the automous systems provided in ISGRI are working correctly to determine and control the presence of the noisy pixels.

A number of permanently noisy pixels in PICsIT were found during subsystem test; there were 36 pixels disabled at the start of PLGC activities, and one more was identified during PLGC tests. During thermal vacuum tests a small number of additional noisy pixels were identified and disabled.

5.3. Detector uniformity

The detector uniformity was assessed during the Laben campaign, before integration with the mask, such that a diffuse background illumination was possible. Figure 9 demonstrates

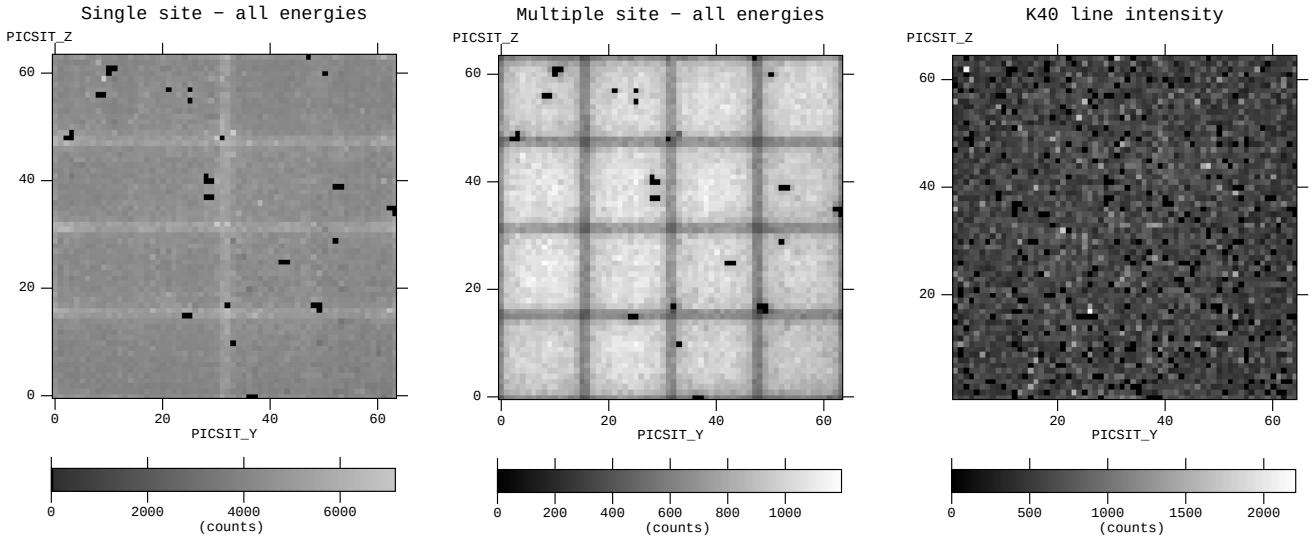

Fig. 9. Edge effects in PICsIT during uniform background illumination: (left) distribution of single-site events; (centre) distribution of multiple-site events; (right) detected counts in the photopeak of the ^{40}K background line.

the non-uniformity of background counts detected across PICsIT, with changes in count rate seen near the edges of modules and semi-modules. Due to the predominance of Compton scattering in the PICsIT energy range, these effects are primarily dominated by the presence of passive material. For single site events, the inter-module material is a source of scattered photons and the count rate is enhanced. For multiple events, the passive material absorbs photons which should have contributed to a multi-site detection, and so multiple events are suppressed. This is also true at semi-module edges since there is no electronic communication between semi-modules and so events which "cross the border" cannot be correctly recorded as multiple-site events.

Figure 9 (right-hand panel) demonstrates that these effects are not an intrinsic non-uniformity in the detectors. This is an image compiled from the intensity of the ^{40}K background line photopeak and is extremely uniform; this confirms that scattering effects in the passive material between modules dominates the non-uniformities seen in the broad-band background.

PICsIT is more susceptible to background non-uniformity effects than ISGRI for a number of reasons: PICsIT operates in an energy regime where Compton scattering is the dominant process; the detectors are thick which emphasises scatter effects; and finally the logic used to record multiple events does not allow communication between all pixels in the detector plane.

6. Efficiency

The efficiency of the IBIS detectors has been assessed as a function of energy as part of the input to the response modelling process, since the efficiency of the detectors across the whole energy range cannot be determined purely by the use of radioactive sources. Indeed the philosophy was always to employ detailed modelling to determine the efficiency, and use the calibration sources to make spot measurements to validate the model.

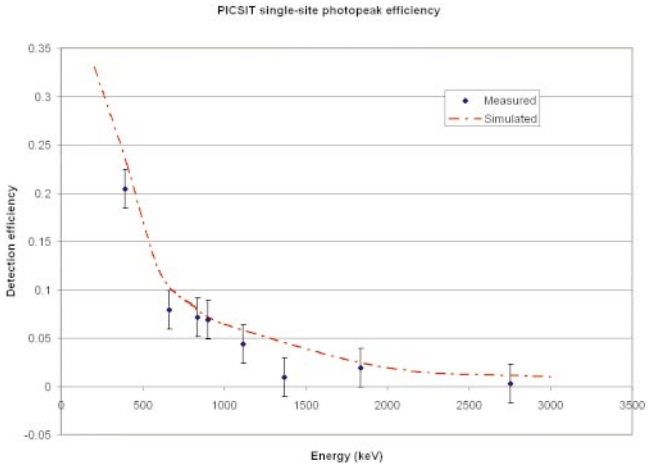

Fig. 10. Photopeak efficiency measured for PICsIT single-site events, compared to simulated efficiency.

For each detection mode, the preferred method is to determine the counts in the detected photopeaks by fitting to the individual pixel spectra. The fit results can then be used to provide good background subtraction, compensation for the presence of the mask, and removal of the effects of broad-band non-uniformities described above.

For ISGRI, due to the complex spectral lineshapes and the varying effective area due to the presence of noisy pixels, the efficiency determination is complex and on-going. However, as an example, and to demonstrate the validity of the efficiency modelling process, the measured photopeak efficiency for PICsIT single-site events is shown in Fig. 10, based on measurements made during the PLGC campaign, and compared to simulations made prior to the tests.

The large uncertainties on the measured efficiency come from a variety of areas including: limited determination of the source activity; solid angle effects due to finite source distance; and imperfect background subtraction. Note also that the contribution of this detection mode to the overall efficiency of IBIS

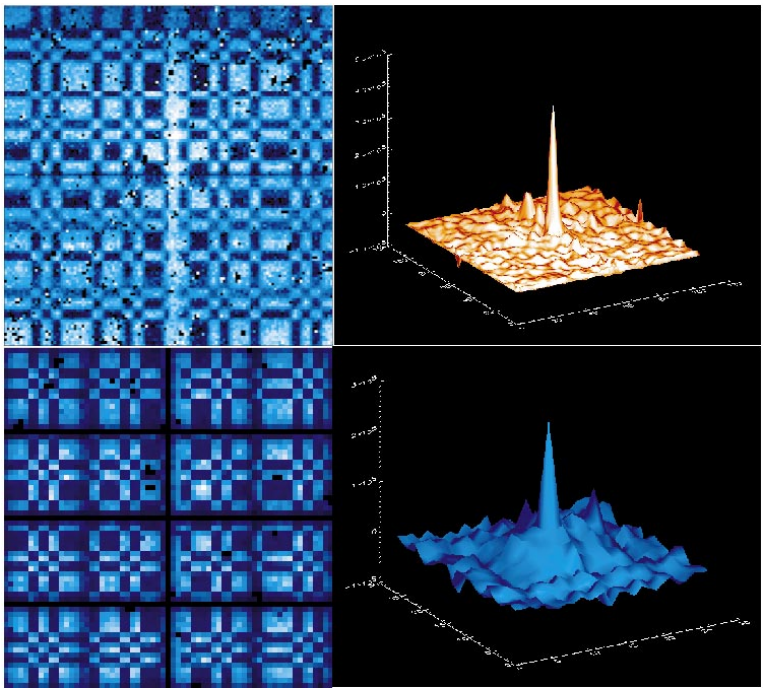

Fig. 11. Imaging response for (top) 17 keV in ISGRI and (bottom) 2.754 MeV in PICsIT. The figures show (left) the recorded shadowgram and (right) the deconvolved image.

is a relatively small one except at low energies. Nevertheless, the degree of agreement is encouraging and there is an ongoing process to improve the consistency of the modelling and measurements.

7. Imaging characteristics

7.1. On-axis response

Simple on-axis imaging tests were performed during the PLGC phase using point sources at a distance of ~5 m from the mask. Shadowgrams and deconvolved images for two sources are shown in Fig. 11, covering the full energy range from below 20 keV (ISGRI image) up to almost 3 MeV (imaged in PICsIT multiple-site events). Note the presence of noisy pixels in the ISGRI image, and the reduced counts at the top of the ISGRI shadowgram caused by the on-ground cooling system. The latter probably introduces some artefacts into the image.

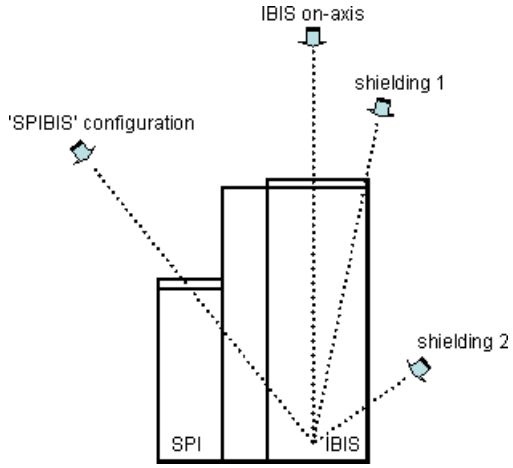

Fig. 12. Off-axis source positions for SPIBIS configuration (see Sect. 7.2), and the shielding tests (see Sect. 8).

7.2. Off-axis response

Measurements were performed during PLGC with a number of off-axis positions/angles such that the IBIS detectors were illuminated through the payload structure in a variety of configurations. These are important configurations to understand since they represent a realistic case for observations: the shadows of strong sources cast by payload structures may hamper the reconstruction of weak sources in the IBIS field of view.

For one specific off-axis case, known as SPIBIS because the SPI mask is projected onto the IBIS detector planes (Fig. 12), the transmission of the intervening material has been measured as a function of energy (Fig. 13). The trend shown in the figure indicates that penetration of the shield and spacecraft structure becomes a more significant factor at high energies, as would be expected.

8. Veto and shielding system

The veto and shielding system, consisting of BGO active veto, hopper, tube and mask was calibrated extensively at subsystem level, and then as part of the integrated IBIS system, where veto-on/veto-off test combinations were frequently employed. However, due to the very different nature of the ground and in-flight backgrounds, the “efficiency” of the shielding system was not explicitly determined during ground calibrations as the result would be largely irrelevant.

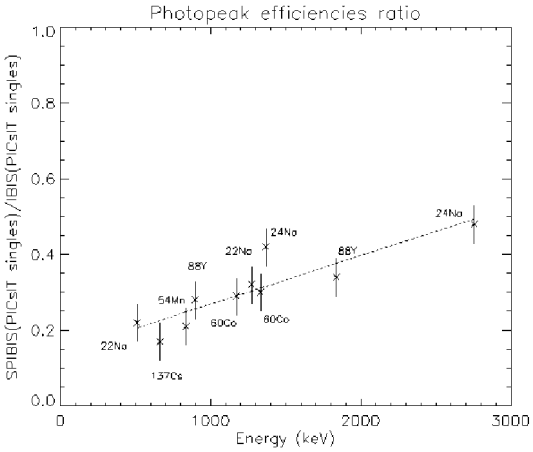

Fig. 13. Transmission at SPIBIS angle, determined by comparison of on-axis (IBIS) and off-axis (SPIBIS) rates.

At subsystem level, the basic detector performances were obtained, and the veto elements were seen to operate well as spectrometers (threshold of 80 keV, energy resolution of 25% FWHM at 662 keV) and remained effective even in the case when only one PMT was operating. The hopper transmission was measured as a function of incidence angle.

A number of shield leakage paths were discovered during pre-calibration and PLGC testing, and these were (wherever possible) blocked with additional lead or tungsten shielding. These are, of course, highly relevant to the in-flight imaging performance. Leakage was discovered through mask mounting holes, around the edge of the mask, and through cable cut-outs in the main detector frame (Fig. 14).

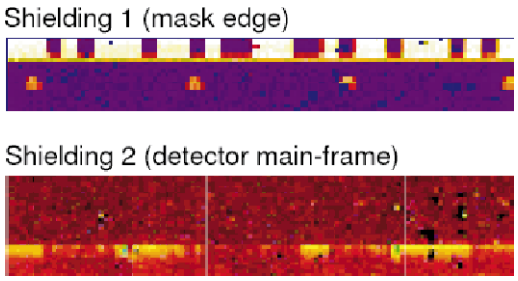

Fig. 14. Leakage paths (top) through the mask surround showing mask pattern and fixing holes, and (bottom) through cable channels in the IBIS mainframe onto the edge of ISGRI. See Fig. 12 for further explanation of the source positions.

Although these leakage paths have been blocked, their presence is still important as fluorescence from the additional shielding will still pass through them. The presence of other leakage paths at this or lower levels cannot be ruled out as there was not enough time to perform a complete scan of the spacecraft at all angles.

9. Conclusions

The many detector systems comprising the IBIS detector have been calibrated in an extensive series of campaigns. Measurements have allowed characterisation of the basic detector characteristics (for each of the 20 000 pixels) and the complex interactions between these components.

The key results obtained from the ground calibration so far have been:

- optimisation of the instrument tunable parameters;
- determination of energy linearity for all detection modes;
- determination of energy resolution as a function of energy through the range 20 keV–3 MeV;
- verification of the Compton mode and the use of background suppression algorithms in that mode;
- demonstration of the imaging capability in each mode;
- measurement of intrinsic detector non-uniformity and understanding of the effects of passive material surrounding the detector plane;
- discovery (and closure) of various leakage paths through the passive shielding system.

The ground calibration results have provided the instrument description tables which are used both on-board and on ground to correct the response from each detector. In combination with sophisticated modelling techniques, the ground calibration data has also helped generate the initial response matrices for IBIS.

The analysis of the IBIS ground calibration data continues (Bazzano 2003), both to understand the instrument better, and in response to specific effects seen in-flight. The PLGC campaign alone recorded some 1.5 billion photons in ~200 different test configurations, so this should provide an archive which will support many future studies.

Acknowledgements. The authors would like to thank all the teams from Laben, Alenia and ESTEC who supported these activities. We also thank U. Zannoni and the FAS team for their technical assistance. Also thanks to Dr J Paul, who campaigned for the payload level calibrations of INTEGRAL, and ultimately lead the activity. The authors acknowledge the national agencies and scientific institutions who have provided financial support through the programme.

References

Bazzano, A., et al. 2003, IBIS Detector Performance During Calibration – Preliminary Results, Proc. PSD6, September 9th–13th 2002, accepted for publication in NIM
Labanti, C., Di Cocco, G., Ferro, G., et al. 2003, A&A, 411, L149
Lebrun, F., Leray, J. P., Lavocat, P., et al. 2003, A&A, 411, L141
Quadrini, E. M., Bazzano, A., Bird, A. J., et al. 2003, A&A, 411, L153
Ubertini, P., Di Cocco, G., Lebrun, F., et al. 1996, SPIE 5-7, 2806, 246
Winkler, C., Courvoisier, T. J.-L., Di Cocco, G., et al. 2003, A&A, 411, L1